Laser Ablation for Diamond X-Ray Optics

Author: Juan José Álvarez Serrano
Supervisor: Frank Seiboth

September 7, 2022

Abstract

Lens material plays a crucial role in the performance of X-ray optics, and diamond has proven to be a highly suitable choice as a result of its unique properties. Its hardness however complicates the fabrication method, for which laser ablation is typically utilized.

In this study, ablation experiments were conducted for CVD Diamond [110] samples. Starting off with simple point-like tests, the relationship between etching rate and laser fluence was evaluated. During this part, two regimes were experimentally observed depending on the amount of removed material: ablation regime for high etching rates, and photooxidation regime for low ones. For the latter, the dependence between the magnitudes was found to be: $r \sim F^{4.63}$, close to the fourth power law reported by previous articles.

An insight into more extensive ablation geometries is also provided, including some initial experimental volume ablation results. Finally, a brief digression on future steps is also commented, to further characterize the method and eventually fabricate diamond lenses.

Contents

1 Introduction

For the past years, the field of X-ray optics has experienced an exceptional growth, marked by the prompt advances in synchrotron radiation sources. Modern and state-of-the-art instrumentation has followed this progress, giving rise to important developments in branches like focusing.

Unlike optical components aimed for visible light, refractive elements for hard X-rays are very difficult to design and manufacture. The main culprits behind this additional strain are the weak refraction and strong absorption of the X-rays inside the lens material.

We can write the index of refraction which defines the X-rays transmission like:

$$n = 1 - \delta + i\beta \tag{1}$$

Where δ is known as the index of refraction decrement, which can be expressed as:

$$\frac{\delta}{\rho} = \frac{N_a r_0 \lambda^2}{2\pi} \cdot \frac{Z + f'(E)}{A} \tag{2}$$

Since $\delta > 0$, we can already see by Equation 1 that the refractive index of X-rays is smaller than one, which means that the vacuum ($n = 1$) is optically denser than the lens material. Therefore, this implies that in order to achieve focusing with X-rays we need to use concave shape lenses.

Another important aspect is that the value of the refraction decrement for X-rays is extremely small. Whereas $|\delta/\rho| \sim 0.2\ cm^3/g$ for visible light, for hard X-rays its value drops to $\sim 10^{-6}\ cm^3/g$. Such a minute value causes the incident and refracted angles to be almost the same, leading to a very large focal distance.

Nevertheless, if we aim for small X-ray beams (little lateral extension), low focal distances are required. To do so one can reduce the radius of curvature of the lens, resulting into a much sharper geometry. However, this method poses the drawback of being technologically very challenging, since it means fabricating a radius of curvature in the micrometer range. A second and more favoured alternative is to work with larger radius of curvature by stacking many of these lenses behind each other. Figure 1 schematically portrays this method, showing how the focal length diminishes as a result of CRL: Compound Refractive Lenses.

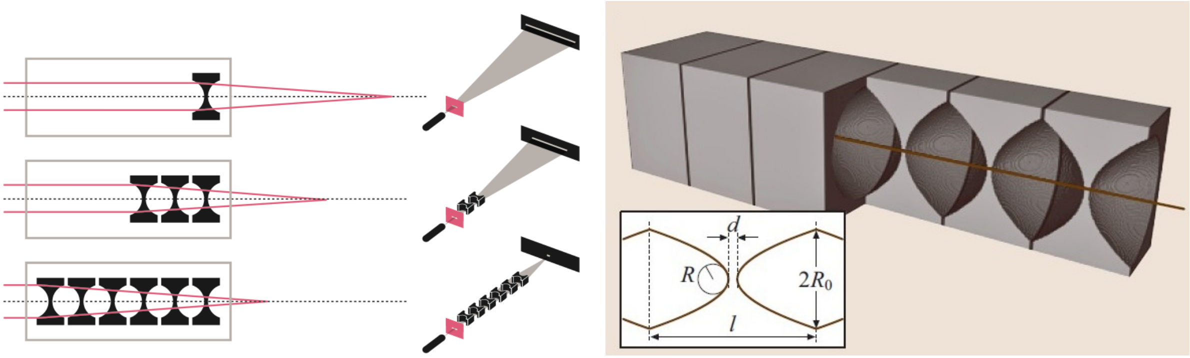

Figure 1: To the left, depiction of how the focal distance decreases as a result of multiple lens stacking, since every lens will bend the beam a little bit. To the right, schematic of a CRL, where R refers to the radius of curvature and $2R_0$ to the aperture of the lens.

As stated in the first paragraph, the absorption of the lens material is another factor that complicates the manufacturing of X-ray lenses. The thicker the material, the fewer the intensity of the transmitted beam in accordance to Beer-Lambert's law:

$$I(x) = I_0 \cdot e^{-\mu x} \tag{3}$$

Minimization of μ in order to obtain maximum transmission is essential, which can be achieved by selecting adequate lens materials. Since $\mu \sim Z^3$ (Figure 2), atomic species with low Z-values are favored, hence the widespread application of beryllium lenses in refractive X-ray studies.

Nonetheless, beryllium counts with certain disadvantages that have motivated the usage of diamond as a promising candidate. Although less transparent to radiation than Be, diamond's refractive index is twice as that of beryllium, thus requiring only half as many lenses to achieve the same focal length. Furthermore, its resistance to big heat loads as a result of a high thermal conductivity avoids the need of powerful cooling, and its single-crystal structure circumvents the appearance of 'speckles' caused by diffuse scattering, as it has been reported to happen in Be lenses.

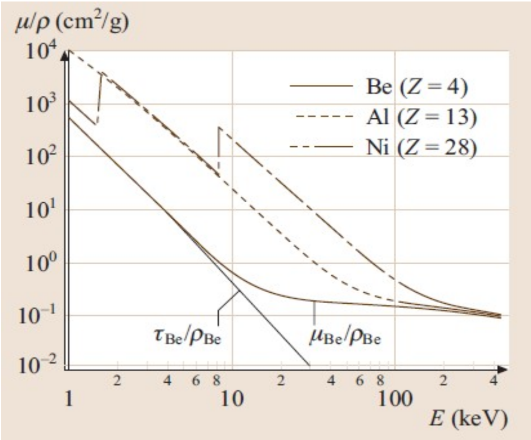

Figure 2: Attenuation coefficient as a function of energy for three different atomic species: Be, Al and Ni.

Despite all the advantages that diamond presents with respect to beryllium, processing of diamond lenses is very complicated due to its hardness. For this reason, femtosecond pulsed lasers have been used for ablation of the diamond plate, shaping it into the form of the desired lens. However this process leaves a relatively rough surface, demanding a necessary post-processing step to polish the lens. Traditionally, this polishing phase has usually been a mechanical method, via a polishing bit.

With this work we look to turn this two-step operation into a single process for the fabrication of diamond lenses. We seek to firstly shape the diamond surface through ablation processes, and using lower energy pulses afterwards (photo-oxidation regime) to reduce roughness. We will also focus on finding and optimizing ablation parameters, so as to achieve a smooth result exempt from graphitization.

If this methodology turns out to be effective, future goals are conceivable in the long run, primarily regarding the fabrication of more diverse lenses and their implementation in large-scale projects like European XFEL.

2 Experimental Method

2.1 Optical Setup

In this section we aim to describe the experimental setup used for the ablation experiments. Figure 3 is a schematic representation of the optical setup, and further information about the characteristics of each optical component can be found in the database of each manufacturer.

The main device is the ultrafast laser {1} *Satsuma HP2* developed by Amplitude®, with some of the most relevant parameters being its central wavelength: $\lambda = 1030nm$, pulsewidth: $\Gamma < 350fs$ and average power: $P > 20W$. We are operating the laser under THG (Third Harmonic Generation), allowing 2 switchable modules at $\lambda = 343nm$.

The first module has a 1 MHz repetition rate with a peak energy of $2\mu J$ per pulse and vertical polarization. The second one works under a repetition rate of 40 MHz at a peak energy of $50nJ$ per pulse with horizontal polarization. Since we are interested in studying laser ablation, only the high-energy module (first module) will be utilized in our work.

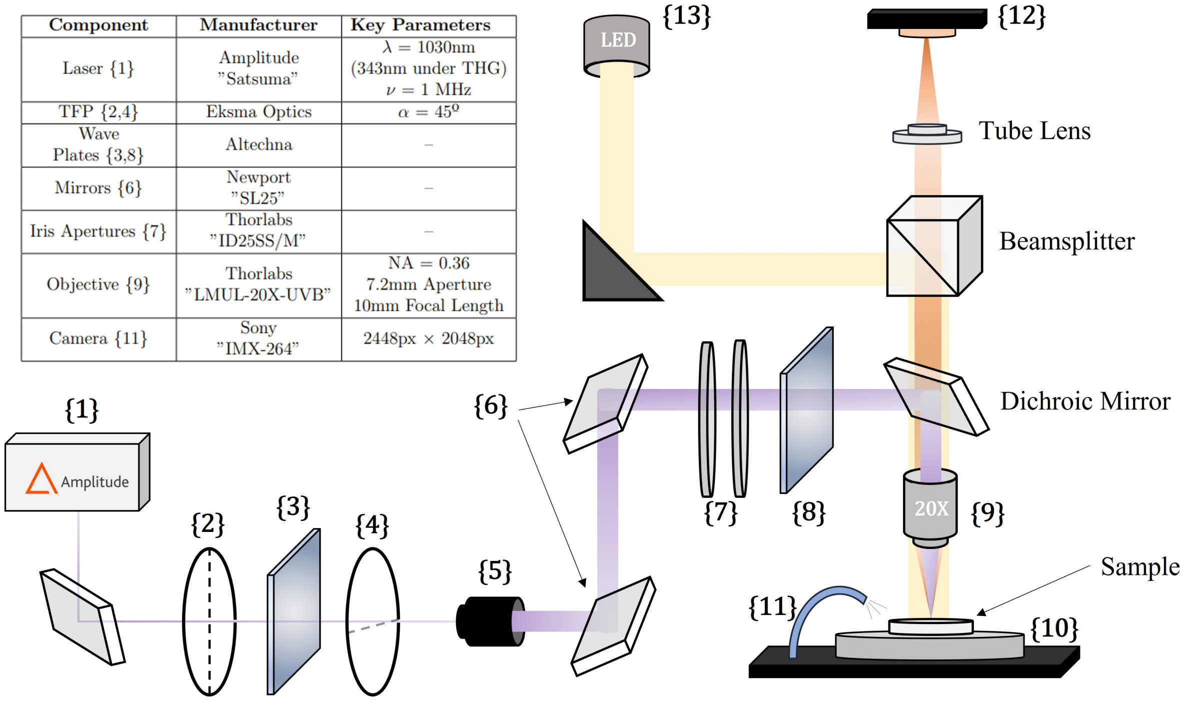

Component	Manufacturer	Key Parameters
Laser {1}	Amplitude "Satsuma"	$\lambda = 1030$nm (343nm under THG) $\nu = 1$ MHz
TFP {2,4}	Eksma Optics	$\alpha = 45^o$
Wave Plates {3,8}	Altechna	–
Mirrors {6}	Newport "SL25"	–
Iris Apertures {7}	Thorlabs "ID25SS/M"	–
Objective {9}	Thorlabs "LMUL-20X-UVB"	NA = 0.36 7.2mm Aperture 10mm Focal Length
Camera {11}	Sony "IMX-264"	2448px × 2048px

Figure 3: Schematic representation of the optical setup, with the key parameters and manufacturer of a series of these items, numbered as referred in the text.

After leaving the module, the laser pulses go through an initial thin film polarizer {2}, a half-wave plate {3} and a second TFM {4}. It is important to highlight the presence of the half-wave plate, as the angle of such wave plate will be the parameter that allows the power to be changed at will, with high precision. This angle is switched via an external software: *DMC*.

After passing through the second TFM, the laser beam reaches an expander {5}, crosses a series of mirrors {6} and iris apertures {7} and arrives at a quarter-wave plate {8}. The quarter-wave plate causes the light to now have circular polarization, which is desired in order to uniformly illuminate the lens following its circular geometry.

After the quarter-wave plate, the beam arrives to the objective {9} with $NA = 0.36$, $7.2mm$ aperture and $10mm$ focal length, and gets focused onto the sample, which lies on top of a motorized stage {10}. This platform can be moved in the X and Y directions thanks to the *DMC* software, and can also be rotated. Even though the mount cannot move vertically, a scan along the Z axis is possible due to the ability of the objective to be dragged along this coordinate. Finally, we also have an air-pressured needle and a suction pump {11} whose role is blowing away and collecting any debris present on the diamond plate during ablation.

In order to see the sample, a CMOS camera *Sony IMX-264* is installed on top of the set-up {12}. A white-light LED {13} is also present to control the brightness with which we can see the sample through the camera.

Figure 4 shows a real image of the experimental set-up, with a zoom on the platform onto which the sample is located during ablation.

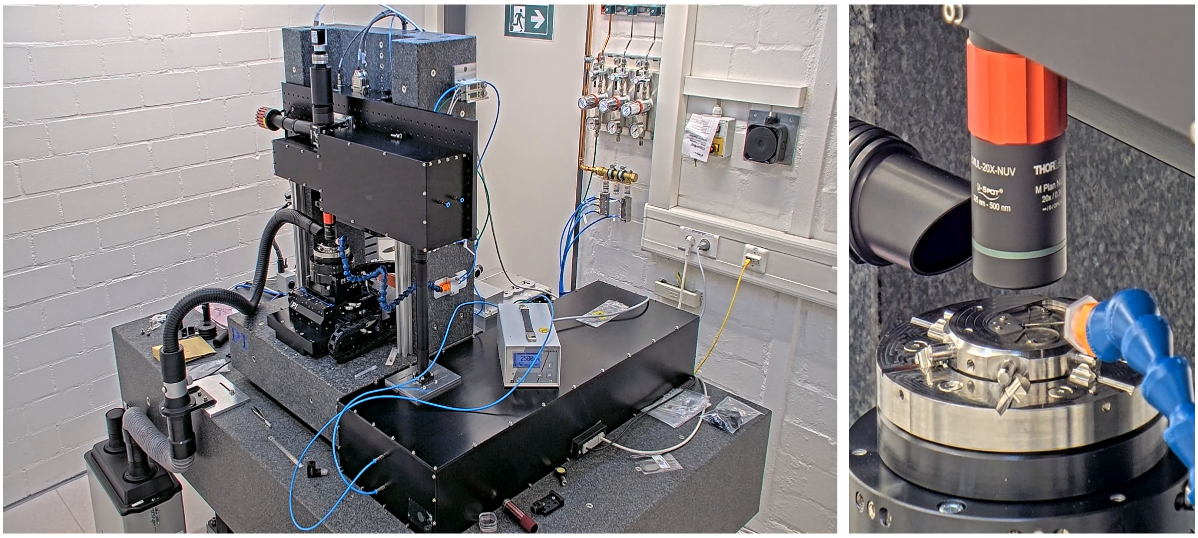

Figure 4: Image of the real experimental setup, with a zoom on the motorized stage and the six-armed mount onto which the diamond sample is placed.

2.2 Measuring Process

All the previous components intervened solely in ablation. Once the sample is ablated, a measuring process must be conducted, since we are interested in finding the most suitable parameters for a smooth, homogeneous and reliable ablation of the diamond surface.

Apart from a qualitative analysis of the result, a quantitative inspection is also necessary to adequately characterize the result. Generally, we aim to find the relation between employed laser fluence and achieved ablation depth, as performed by other authors. The former was typically measured based on the power readings of a PM-10 diode and the subsequent physical relations linking power to energy. The latter was quantified thanks to the laser microscope *Keyence*, although Atomic Force Microscopy was also occasionally used. The reason behind utilizing an AFM was the lack of resolution or poor reliability in some measurements done with the laser microscope, especially when the hole had very steep and abrupt boundaries.

3 Results and Discussion

3.1 Relation between Laser Fluence and Etching Rate

Our main goal describing the ablation process is to link etching rate and laser fluence. This relation has been recorded by authors like Kononeko et al. [5], whose results are presented in Figure 5. They predict two different regimes according to the relation between these two magnitudes: ablation and photooxidation. Whereas in the ablation regime etching rate depends weakly on λ, in photooxidation the difference between wavelengths is very clear.

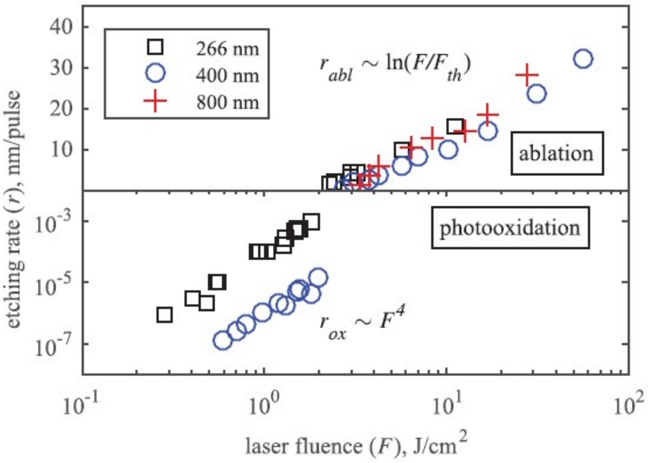

Figure 5: Etching rate (r) as a function of laser fluence (F) for three different wavelengths. Extracted from [5].

Etching rate is defined as the depth of the ablated hole per number of fired pulses, so to know this variable we must count the number of fired pulses and measure the height of the hole.

As stated in previous sections, pulse energy density cannot be measured directly. We can arrive to its value once known the power and the width of the beam:

$$F = \frac{1}{\nu} \cdot \frac{P}{\pi \omega^2} \tag{4}$$

Where we assume that we are always working in the focus, and we divide over the frequency to express the fluence of each pulse.

In summary, for us to create a similar plot as Figure 5 we will need four variables: power, number of pulses, beam width and hole depth.

3.1.1 Power Readings

As discussed in the previous section, power was measured thanks to a PM-10 diode, and changes in the read power came as a result of changes in the angle of the wave plate.

Power (and ultimately laser fluence) can also be desirably modified by changing the AOM transmission rate, however this second method is less reliable since the fluctuations in the transmission rate provide a greater experimental error. Therefore, power variations in our experiments have always been originated through changes in the wave plate at a fixed transmission rate.

Power measurements and laser ablation could not be done simultaneously, since both the diode and the sample would have to be located in the same place under the objective. Therefore we have first obtained the dependence of power with the angle of the wave plate, and then we run ablation tests under different angles of the wave plate. This way we avoid having to constantly swap between sample and diode for every measure.

Figure 6 shows the dependence of power (normalized) with the angle of the wave plate. Additionally, later in the experiment we have restricted ourselves to only scan along angles where the relationship between these two magnitudes is somewhat linear, to minimize error. For the most part, the angular range we have used has been from 45° to 63° for a fixed value of the transmission rate of 4.5%, which corresponds to variations in power from $9.34mW$ to $36.46mW$.

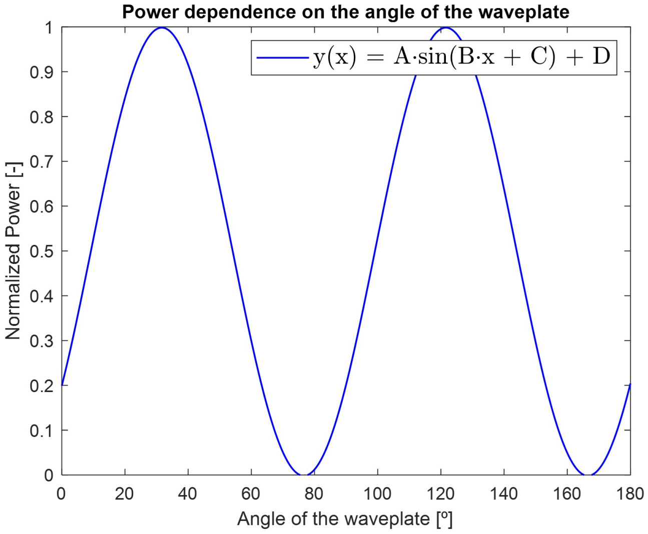

Variable	Value
A	0.500
B	0.070
C	5.642
D	0.498

Figure 6: Power (normalized) dependence on the angle of the wave plate. The analytical best-fit expression is presented in the legend, with the value of the parameters in the table aside.

3.1.2 Number of Pulses

The number of pulses can be directly specified at the *DMC* software. However, we have observed that certain anomalies occurred, as in some situations the inserted values did not match the amount of real pulses. For this reason, whenever it was possible and sensible, we doubled-checked this variable thanks to an oscilloscope.

We believe this irregularities appeared due to a time delay present in the software, of $t = 1ms$. As a result of this delay, when working with high frequencies we expect a bigger pulse difference than when working at lower frequencies, since at high frequencies more undesired pulses can go through during that millisecond; something also experimentally observed. For example, when $\nu = 1000\text{Hz}$, 1 expected pulse turned out to be 10 real pulses, whereas when the trigger frequency was lowered to $\nu = 100\text{Hz}$, 1 expected pulse turned out to be 2 real pulses.

3.1.3 Beam Width

Assuming we are always working in the focus, this parameter can be calculated through the optical relation:

$$w_0 = \frac{1}{2} \cdot \frac{4\lambda f M^2}{\pi D} \tag{5}$$

Where λ corresponds to the wavelength, f to the focal length, M^2 to the beam quality parameter and D to the beam diameter at the lens, which is restricted by the lens aperture. For our experiment, $\lambda = 343nm$, $f = 10mm$, $M^2 = 1.09$ and $D = 7.2mm$, resulting into a beam radius of $\underline{w_0 = 331nm}$.

However, in order to also connect with our ablation results, we have constructed a simple model to extract the value of w_0 based on the opening size of individual ablated holes and the power under which they were ablated.

The intensity distribution of the laser beam is Gaussian, so it can be expressed as:

$$I(r,z) = I_0 \cdot \left(\frac{w_0}{w(z)}\right)^2 \cdot e^{-\frac{2r^2}{w(z)^2}} \tag{6}$$

Since we are always under the assumption of operating at focus ($z = 0$), Equation 6 can be simplified to:

$$I(r,0) = I_0 \cdot e^{-\frac{2r^2}{w_0^2}} \tag{7}$$

In our model, we are based on the idea that for the process of ablation to occur, a certain intensity threshold I_T must be surpassed. As presented before, for a fixed z value, the laser's intensity profile peaks at $r = 0$, and will decrease for larger radial values. Therefore, for a hole of any given size, every position such that $r < R$ (with R the radius of the hole) corresponds to regions where intensity was above the threshold, whereas R indicates the position where the intensity equalled the threshold, as no ablation was observed for further radial values. This idea is illustrated in Figure 7.

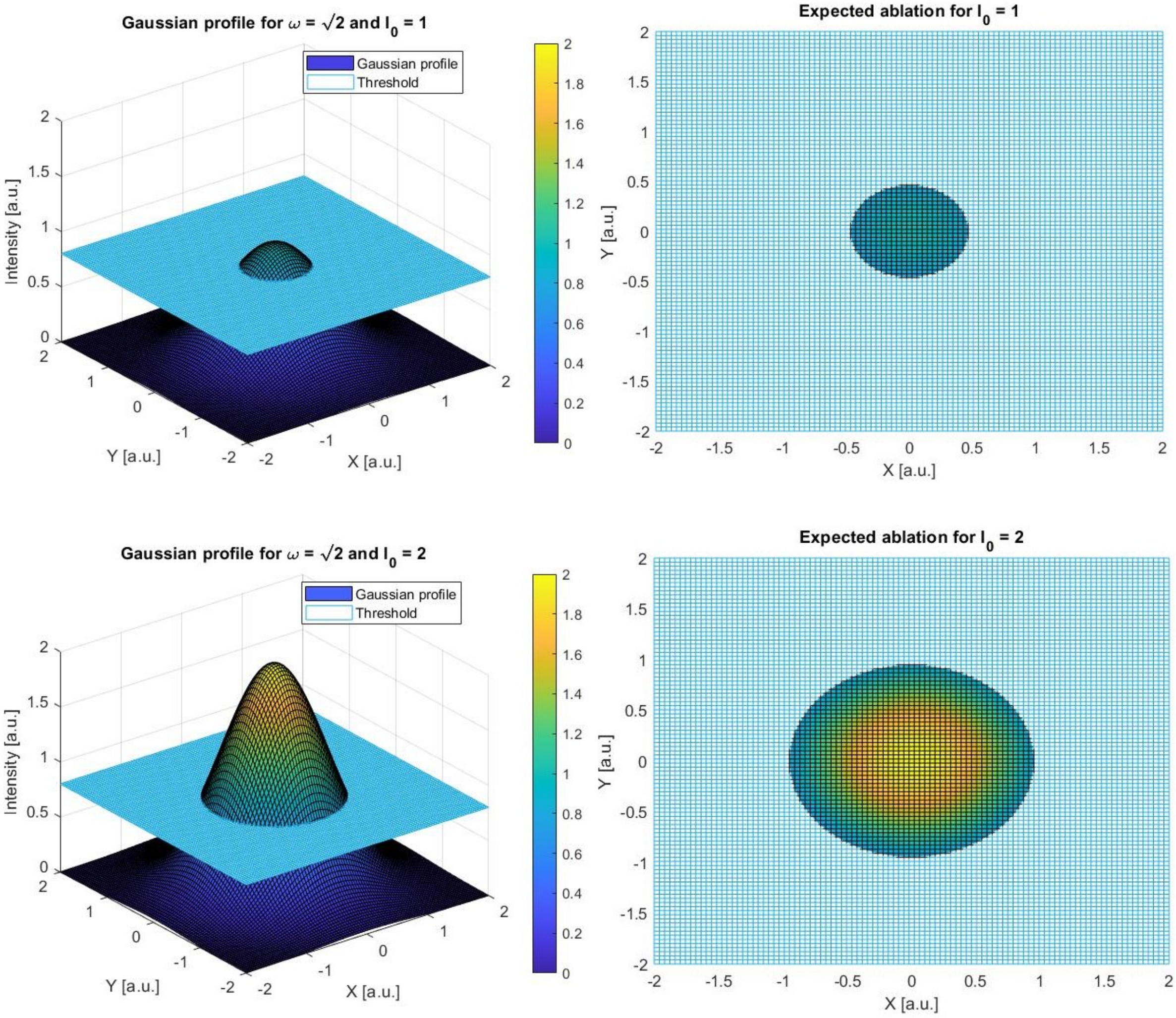

Figure 7: To the left, intensity distributions for the cases of $w_0 = \sqrt{2}$ and $I_0 = 1$ (top figure) and $I_0 = 2$ (bottom figure). For low intensities only the values near $r = 0$ are over the ablation threshold, thus expecting a "small" opening size for the ablated hole, as it can be seen from the image to the right. For the case of high intensities we expect the size of the circle to increase, as bigger radial values also surpass the ablation threshold.

When increasing the power, we are increasing the amplitude of the Gaussian that describes the intensity profile, allowing for the threshold to be reached at higher radial values. However the beam width does not change, allowing us to estimate its value based on comparisons of every pair of ablated holes.

Following with this idea, the intensity at the edges of any hole has to be equal to the threshold, so given holes i and j, it must be fulfilled that:

$$I_T = I_i(R_i) = I_j(R_j) = I_{0,i} \cdot e^{-\frac{2R_i^2}{w_0^2}} = I_{0,j} \cdot e^{-\frac{2R_j^2}{w_0^2}} \tag{8}$$

Solving for w_0 we can arrive at:

$$w_0 = \sqrt{\frac{2(R_i^2 - R_j^2)}{\log(I_{0,i}/I_{0,j})}} = \sqrt{\frac{2(R_i^2 - R_j^2)}{\log(P_i/P_j)}} \tag{9}$$

Where we have used that:

$$\log\left(\frac{I_{0,i}}{I_{0,j}}\right) = \log\left(\frac{P_i}{P_j}\right) \tag{10}$$

Because the definition of power: $dP = I \cdot dA$ allows us to relate the power and the intensity at the peak of the Gaussian as:

$$P = \int_0^{2\pi} \int_0^{\infty} I(r) \cdot r dr d\theta = \int_0^{\infty} 2\pi I_0 e^{-\frac{2r^2}{w_0^2}} \cdot r dr = \frac{I_0 \pi w_0^2}{2} \tag{11}$$

And, since the beam width stays constant, we observe that indeed the quotient between intensities at the peak is equal to the quotient between powers.

Figure 8 shows the experimental results, with a table aside that gathers the average value for configurations with different number of shots per point. In general, it can be seen how the values are close to each other, but far away from the value we had initially calculated through optical relations. One possible explanation could be not working exactly on focus like we are assuming, but slightly out of it. For instance, for a separation of $1.5\mu m$ the width of the beam already rises to $633nm$, according to the waist evolution of a Gaussian beam:

$$w(z) = w_0 \cdot \sqrt{1 + \left(\frac{z}{z_R}\right)^2} \tag{12}$$

With $z_R = \frac{\pi w_0^2}{\lambda M^2}$ the Rayleigh range.

This deviation from the focus can also come as a result of a tilt of the diamond plate, as it was experimentally observed that the camera focal plane (thus, the laser focal too) slightly changed along the ablated region.

Another possible reason could have to do with fluctuations in power. This means that a small amount of pulses get fired at a higher power than what we assume, thus ablating a wider region and creating a hole with a bigger opening size.

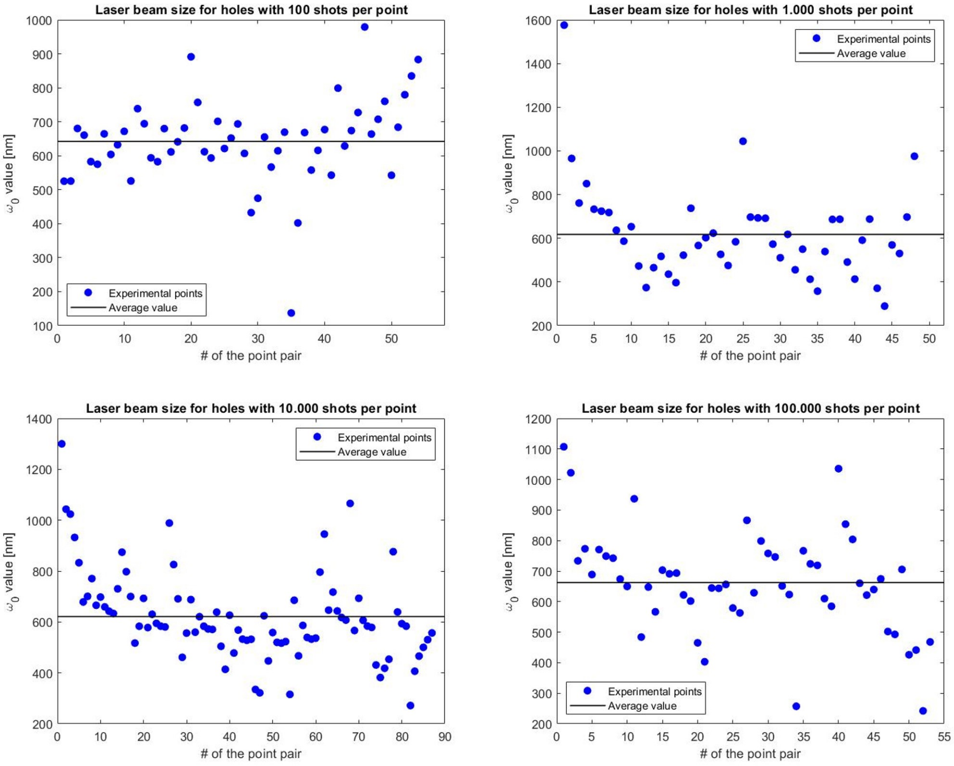

Laser beam size for holes with 100 shots per point

Laser beam size for holes with 1.000 shots per point

Laser beam size for holes with 10.000 shots per point

Laser beam size for holes with 100.000 shots per point

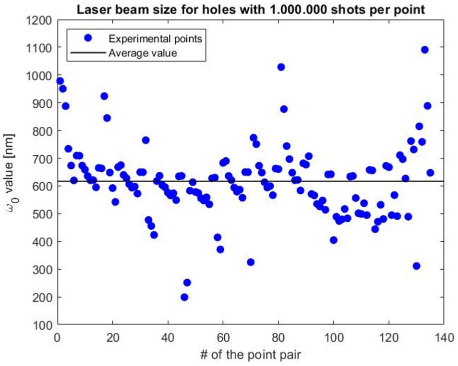

Laser beam size for holes with 1.000.000 shots per point

	Beam Radius [nm]
100 Shots/Point	642
1K Shots/Point	617
10K Shots/Point	622
100K Shots/Point	663
1M Shots/Point	617

Figure 8: Experimental w_0 values obtained from the comparisons of ablated hole pairs. The table aside contains the numerical values for each configuration, where K stands for thousand and M for million.

3.1.4 Depth Measurement

As mentioned in the section regarding the measuring process, Atomic Force Microscopy was occasionally used in order to quantify with high precision the depth of individual holes.

An example was when inspecting ‘tiny’ holes, noticeable with the AFM but invisible when using the laser microscope. Figure 9 is an example of one of these holes, together with the measured height profile. These kind of holes were generated at very low powers and a high number of pulses per point, thus corresponding to the so called photoxidation regime from Figure 5.

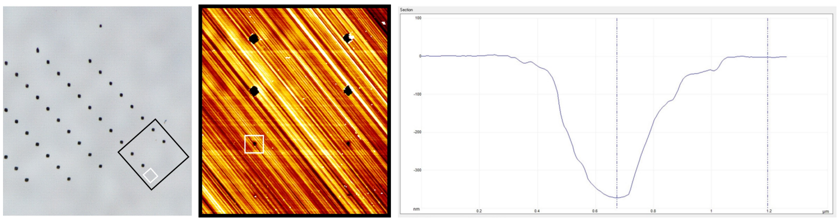

Figure 9: Height profile of an ablated hole, calculated through AFM.

Figure 10 shows the experimental results when combining the measured depths of many different holes, and the laser fluence at which they were generated. The plot also contains the best-fit to the empirical values, where the obtained relation between etching rate and laser fluence scales as $r_{ox} \sim F^k$ with $k = 4.63$, a value not far away from the recorded by Kononenko et al. [5], where $k_{Kon.} = 4$.

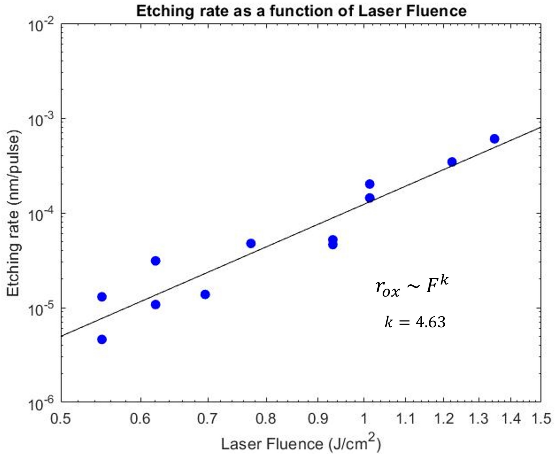

Figure 10: Etching rate as a function of laser fluence. The experimental result for the power dependance between etching rate and laser fluence is close to the reported value by Kononenko et al. [5] in the photooxidation regime.

In order to recreate the relation portrayed in Figure 5 completely, results regarding ablation regime must also be analyzed. This configuration corresponds to more intense pulses, that remove more material from the substrate. Holes in this regime have a much bigger opening size and therefore are clearly visible with the laser microscope *Keyence*, allowing us to measure their depths directly with this tool.

However, we realized that depth measurements with the laser microscope were not reliable, since we obtained very dissimilar results when changing the optical magnification. This is illustrated in Figure 11, where the measured depth of one random hole is almost doubled when changing the magnification from 50× to 100×. Although the origin of such limitation in the depth determination is not clear, we suggest that it may arise from the abrupt change in height for a still very small region.

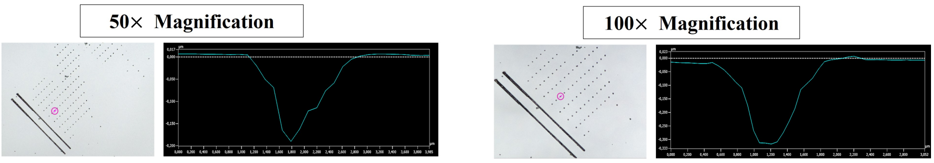

Max. Depth: 176 *nm*

Max. Depth: 316 *nm*

Figure 11: Depth measurement of a certain hole depending on the magnification.

Therefore, in order to precisely characterize the dependence of etching rate and laser fluence in the ablation regime, measurements with an AFM should also be conducted. Figure 12 is the superposition of the experimental results from the photooxidation regime (presented in Figure 10) with some results corresponding to the ablation regime that we had the chance to measure with the AFM. Nevertheless, many more points are required.

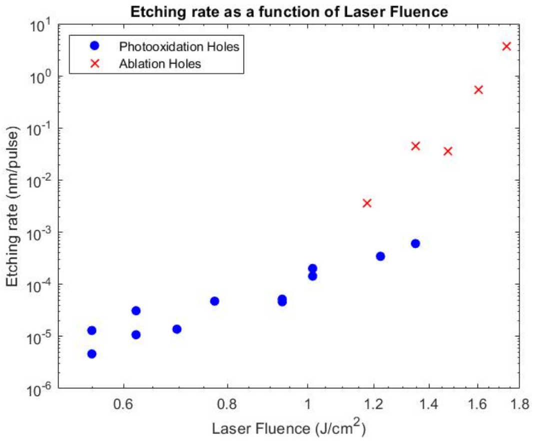

Figure 12: Etching rate as a function of laser fluence for photooxidation (blue) and ablation (red) regime.

3.2 Area and Volume Ablation

Many parameters are involved in the ablation process of larger shapes and geometries. Together with power, some other relevant parameters are:

- Pulse Burst: It is the number of bursts (fired shots) for every given spatial position.
- Spacing: It is the separation between consecutive contours in an area ablation experiment. For instance, if we want to ablate a circular area, the spacing would be the separation between each circunference that fills the circle.
- Pulse Pitch: It is the spatial separation between consecutive points for a one-dimensional ablation experiment. For instance, if we want to ablate a circular area, the pulse pitch would be how far apart is one position and the next one from each of the circunferences that fill in the circle.

Our *modus operandi* has been trying to find what combination of values give the best result in one-dimensional (line) ablation experiments, and use these values to perform higher dimensionality experiments.

As illustrated by Figure 13, some combination of values that worked for line ablation experiments turned out to cause damage when performing area ablation: {A}, while others worked for both 1D and 2D analysis: {B}.

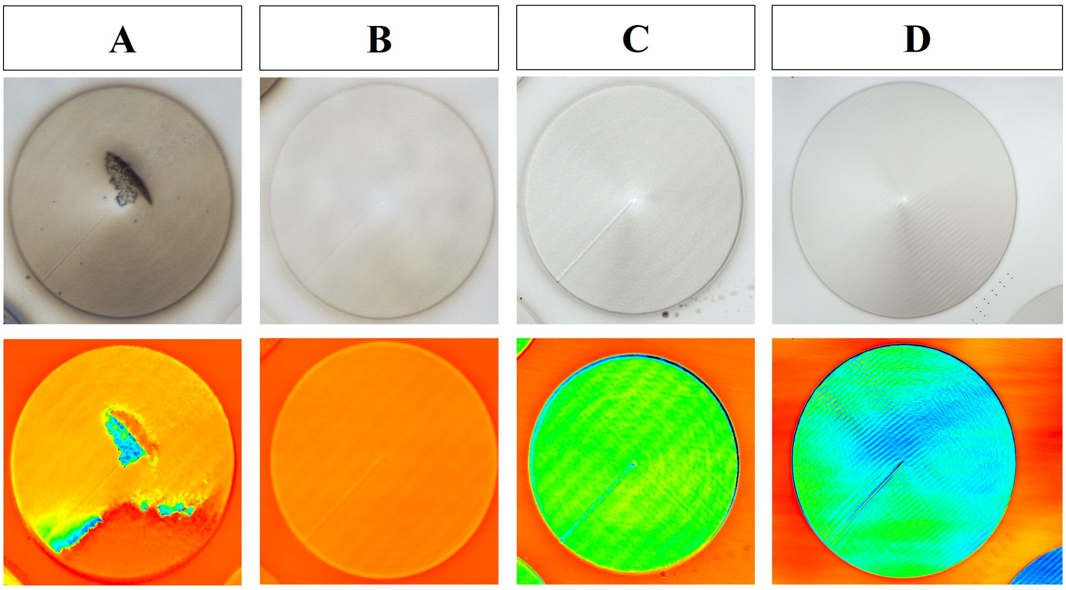

Figure 13: Optical image (top) and height profile (bottom) for area ablation configurations with different combination of parameters.

After selecting only the ones that achieved a smooth and homogeneous result, a series of tests were conducted increasing the speed of the platform. This step was carried out to filter and pick only those who also worked for high speeds: {C} and {D}, so as to ablate in the future large areas and volumes in reasonable times.

The configuration used in {B}, {C} and {D} in Figure 13 achieved a surface roughness in the order of tenths of nanometers, while also avoiding graphitization of the area. This can be told by the aspect of the ablated surface, which preserves a similar whitish/grayish color as the diamond sample.

With the parameters studied during area ablation experiments we conducted the first volume ablation analysis, whose results are presented in Figure 14. The shape corresponds to paraboloids with equation:

$$z = \frac{r^2}{2R_0} \tag{13}$$

Where these first results were performed for values of the curvature $R_0 = 50\mu m$, height spacing $= 240nm$ and total height $h = 25\mu m$.

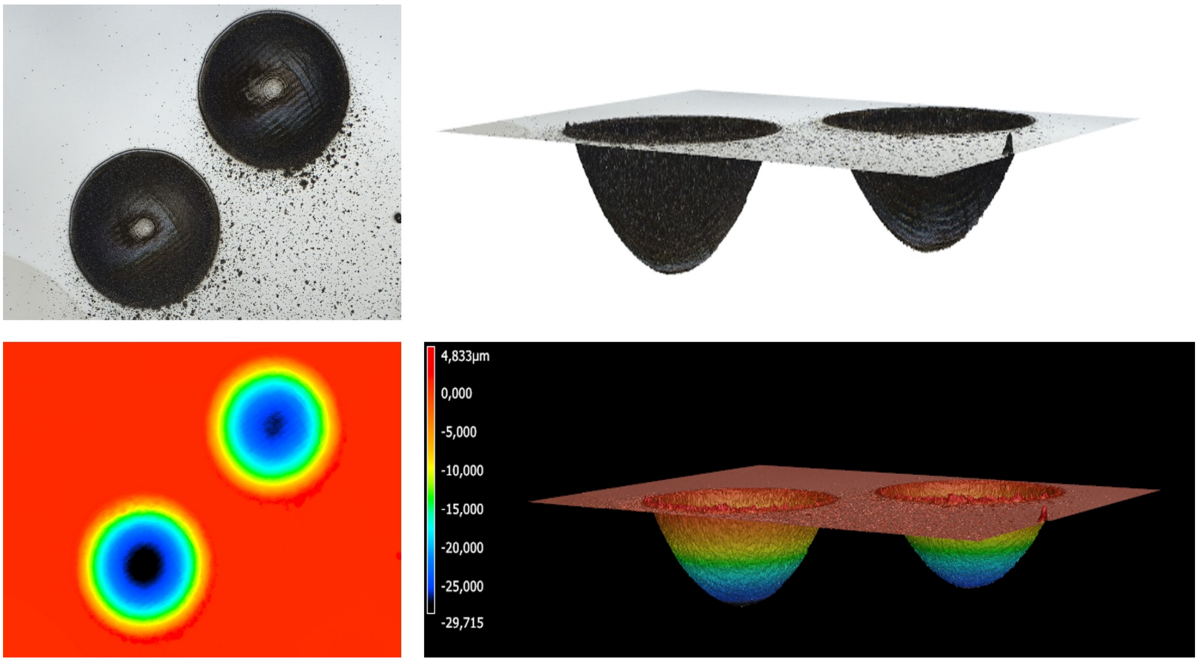

Figure 14: First volume ablations. The figures in the top correspond to the laser microscope images, while the ones in the bottom are the height measurements. It can be seen how in the optical image some debris is present in the sample as a result of ablation.

Looking through the microscope after ablation, it can be seen how some debris is present in the surface as a result of the ablation process. It is accumulated according to the air flow provided by the pressurized needle, and not all the fragments get collected by the suction pump. Since the pump cannot be located any closer to the sample due to the limited space there is, a possible solution would be changing the air mechanism to blow the debris away directly from top (in the same direction as the beam that is ablating the diamond).

Another observation is that the ablated volume is very dark compared to the surface of the diamond. This is an evidence of graphitization taking place, which means that the outline of the paraboloid has carried out a phase transition: from diamond to graphite. This is something undesired, but could be corrected via two different mechanisms. On the one hand, more experiments with new parameters could be carried out, until we observe an outcome free of graphitization. A second option could be conducting an ablation process over the results we have so far, but this time ablating only over the contour of the paraboloid. The idea behind this alternative is to remove the external graphite layer and be left with the diamond beneath.

Finally, one last interesting verification would be to see how much this experimental ablation differs from a paraboloid mathematically described by Equation 13. This process cannot be done with the microscope software, but it could be achieved through any external data analysis program, using the least squares method.

4 Conclusions and Next Steps

We have achieved ablation for CVD diamond samples under different configurations, optimizing the parameters and presenting the best combination of values to reach a high-quality result for each case. Our study has also included the analysis of the etching rate as a function of laser fluence, with clear observations of both an ablation and photooxidation regime. For the latter, the relation between these magnitudes has been found to scale as a power law, with the exponent: $k = 4.63$ close to the reported value from other authors.

Some more immediate steps to expand our study include studying the dependence of etching rate and laser fluence for the ablation regime through precise AFM hole-depth measurements, or further investigating and characterizing volume ablation through some initiatives like the ones suggested at the end of Section 3.2. After this evaluation, a subsequent implementation of photooxidation to reduce surface roughness would also be of the greatest interest.

As for the long run, we contemplate extending this methodology to fabricate more diverse lenses, and studying their focusing performance when placed in a X-ray beam line.

5 Acknowledgements

I would like to convey my sincere thanks to my supervisor Frank Seiboth as well as PhD student Wenxin Wang, who provided great support and valuable guidance during the whole project. I also would like to express my gratitude towards the FS-PETRA group for the warm reception into their team, and to all the DESY organization members for arranging everything necessary and offering their assistance throughout this summer internship program.

References

[1] Träger, F. (2007). *Springer Handbook of Lasers and Optics*. Part D, Chapter 18. Springer Publishing.

[2] Terentyev, S., Polikarpov, M., Snigireva, I., di Michiel, M., Zholudev, S., Yunkin, V., Kuznetsov, S., Blank, V., Snigirev, A. (2017). *Linear parabolic single-crystal diamond refractive lenses for synchrotron X-ray sources*. Journal of Synchrotron Radiation, **24**, 103–109.

[3] Celestre, R., Antipov, S., Gomez, E., Zinn, T., Barrett, R., Roth, T. (2022). *Polished diamond X-ray lenses*. Journal of Synchrotron Radiation, **29**, 629–643.

[4] Ramanathan, D., Molian, P. A. (2002). *Micro- and Sub-Micromachining of Type IIa Single Crystal Diamond Using a Ti:Sapphire Femtosecond Laser*. Journal of Manufacturing Science and Engineering, **124**, 389–396.

[5] Kononenko, V. V., Gololobov, V. M., Komlenok, M. S., Konov, V. I. (2015). *Nonlinear photooxidation of diamond surface exposed to femtosecond laser pulses*. Laser Physics Letters, **12**, 096101.